ectoderm, can be divided into two distinct domains (Fig. 4). The dorsal AER is characterized by the presence of AER-specific markers, whereas the ventral AER is distinguished by the additional expression of En-1. Loss of En-1 function appears to allow a ventral expansion of the AER. In this situation, the Wnt-7a-negative region at the distal tip of the mutant limbs might be analogous to the dorsal wild-type AER, whereas the ectoderm expressing Wnt-7a in addition to AER-specific markers might represent the ventral AER. Alternatively, the distal Wnt-7a-negative ectoderm might demarcate the entire functional domain of the AER, but several pieces of evidence suggest that this is not the case. Both morphological criteria and gene-expression

data suggest that the AER extends beyond the ventral boundary of the Wnt-7a-negative domain. Furthermore, preliminary studies suggest a parallel proximoventral expansion of progress zone markers (data not shown). Finally, limb structures that normally develop only distally were duplicated proximoventrally in En-1 mutant mice, a phenotype consistent with a functional expansion of the AER. Thus our data indicate that En-1 is required for delineating the ventral AER boundary and for restricting expression of signalling molecules, such as Fgf-8 and Bmp-2, to the distalmost ectoderm, a function reminiscent of engrailed's role in compartment border formation in Drosophila[18-20].   □

1. Johnson, R. L., Riddle, R. D. & Tabin, C. Curr. Opin. Genet. Dev. 4, 535–542 (1994).
2. Tickle, C. Curr. Opin. Genet. Dev. 5, 478–484 (1995).
3. Martin, G. R. Nature 374, 410–411 (1995).
4. Parr, B. A. & McMahon, A. P. Nature 374, 350–353 (1995).
5. Riddle, R. D. et al. Cell 83, 631–640 (1995).
6. Vogel, A., Rodriguez, C., Warnken, W. & Izpisua Belmonte, J. C. Nature 378, 716–720 (1995).
7. Davis, C. A. & Joyner, A. L. Genes Dev. 2, 1736–1744 (1988).
8. Joyner, A. L. & Martin, G. R. Genes Dev. 1, 29–38 (1987).
9. MacCabe, J. A., Errick, J. & Saunders, J. W. Jr Devl Biol. 39, 69–82 (1974).
10. Patau, M.-P. in Vertebrate Limb and Somite Morphogenesis (eds Ede, D. A., Hinchliffe, J. R. & Balls, M.) 257–266 (Cambridge Univ. Press, 1977).
11. Geduspan, J. S. & MacCabe, J. A. Devl Biol. 124, 398–408 (1987).
12. Geduspan, J. S. & MacCabe, J. A. Anat. Rec. 224, 79–87 (1989).
13. Wurst, W., Auerbach, A. B. & Joyner, A. L. Development 120, 2065–2075 (1994).
14. Hanks, M., Wurst, W., Anson-Cartwright, L., Auerbach, A. B. & Joyner, A. L. Science 269, 679–682 (1995).
15. Lyons, K. M., Pelton, R. W. & Hogan, B. L. M. Development 109, 833–844 (1990).
16. Crossley, P. H. & Martin, G. R. Development 121, 439–451 (1995).
17. Parr, B. A., Shea, M. J., Vassileva, G. & McMahon, A. P. Development 119, 247–261 (1993).
18. Sanicola, M., Sekelsky, J., Elson, S. & Gelbart, W. M. Genetics 139, 745–756 (1995).
19. Zecca, M., Basler, K. & Struhl, G. Development 121, 2265–2278 (1995).
20. Tabata, T., Schwartz, C., Gustavson, E., Ali, Z. & Kornberg, T. B. Development 121, 3359–3369 (1995).
21. Lufkin, T. et al. Nature 359, 835–841 (1992).
22. Wilkinson, D. G., Bailes, J. A. & McMahon, A. P. Cell 50, 79–88 (1987).
23. Lyons, K. M., Pelton, R. W. & Hogan, B. L. M. Genes Dev. 3, 1657–1668 (1989).

Influence of dendritic structure on firing pattern in model neocortical neurons

Zachary F. Mainen* & Terrence J. Sejnowski

Howard Hughes Medical Institute, Computational Neurobiology Laboratory, Salk Institute for Biological Studies, La Jolla, California 92037, and Department of Biology, University of California, San Diego, La Jolla, California 92093, USA

NEOCORTICAL neurons display a wide range of dendritic morphologies, ranging from compact arborizations to highly elaborate branching patterns[1]. In vitro electrical recordings from these neurons have revealed a correspondingly diverse range of intrinsic firing patterns, including non-adapting, adapting and bursting types[2,3]. This heterogeneity of electrical responsivity has generally been attributed to variability in the types and densities of ionic channels. We show here, using compartmental models of reconstructed cortical neurons, that an entire spectrum of firing patterns can be reproduced in a set of neurons that share a common distribution of ion channels and differ only in their dendritic geometry. The essential behaviour of the model depends on partial electrical coupling of fast active conductances localized to the soma and axon and slow active currents located throughout the dendrites, and can be reproduced in a two-compartment model. The results suggest a causal relationship for the observed correlations between dendritic structure and firing properties[3-7] and emphasize the importance of active dendritic conductances in neuronal function[8-10].

We began with a compartmental model used in a previous study of spike initiation[8]. This model included a low density of Na+ channels in the soma and dendrites[11] and a high density in the axon hillock and initial segment[12,13]. Fast K+ channels were present in the axon and soma but excluded from the dendrites. To extend the

model from single spikes to spike trains, slow K+ channels responsible for the spike afterhyperpolarization (AHP) and control of repetitive firing[14,15] (both calcium-dependent and voltage-dependent) were added to the soma and dendrites, along with one type of high-threshold Ca2+ channel.

Dendritic arborizations were designed using reconstructions of neocortical neurons with a variety of morphologies (Fig. 1). When simulated with the same channel types and densities, a range of distinct firing patterns was produced. Firing patterns correlated strongly with the extent of arborization and, to the degree that it was correlated with morphology, with the cell layer. Smooth stellates (n = 4), with the smallest dendritic arborizations, produced spike trains with deep, monophasic AHPs and very weak spike-frequency adaptation (Fig. 1a). Layer 4 spiny stellates (n = 5), with somewhat larger dendritic trees, gave adapting spike trains (Fig. 1b). Still more extensive layer 2 and 3 pyramidal neurons (Fig. 1c) showed spike after-depolarizations (ADPs) along with doublet or burst firing. The largest cells, layer 5 pyramidal neurons (n = 7), produced repetitive bursting spike trains (Fig. 1d). Although the specific set of patterns produced across this set of cells could be altered by changing the channel densities, the correlation between dendritic structure and firing pattern was insensitive to variations in the choice of channel kinetics and channel densities, as long as the basic regional segregation of fast and slow channel types was maintained. The results also seemed robust to heterogeneity of channel densities within the dendritic tree (as suggested by physiological studies[16,17]), although such scenarios were not examined exhaustively.

To facilitate analysis of the role of dendritic electrical structure in shaping firing behaviour, a reduced two-compartment version of the model[18] was examined (Fig. 2a). In this reduced model, electrical structure was determined by just two parameters: the ratio of axo–somatic area to dendritic membrane area (ρ) and the coupling resistance between axo–somatic and dendritic compartments (κ). These parameters were systematically varied while holding channel densities constant. When uncoupled ($\kappa \to \infty$), simple stereotyped oscillatory patterns were generated in the two compartments (Fig. 2b), with the axo–somatic compartment having a much higher intrinsic frequency owing to its relatively

rapid channel kinetics. When the dendrite and axon–soma were fully coupled ($\kappa \to 0$), alteration of ρ affected the size of AHP and the amount of spike-frequency adaptation, but produced a limited set of firing properties (Fig. 2c).

A weak to moderate coupling strength was necessary to produce the full range of firing patterns, including spike bursts and ADPs. With such partial coupling, small changes in ρ or κ produced dramatic changes in firing pattern (Fig. 2d, e). Dendritic Na$^+$ channels were critical to the generation of bursts and ADPs[6,19,20] (Fig. 3a–c). These channels promoted propagation of spikes from the axon–soma into the dendrite, by prolonging the depolarization following a spike[21]. After the soma and axon had repolarized, current returned from the dendrite to produce a late depolarizing transient (the ADP), with somatic spike bursts occuring when ADPs were above threshold[22]. Decreasing κ or ρ suppressed bursting and ADPs by reducing the delayed depolarization associated with the dendritic spike (Fig. 3d, e). In addition, factors that affected the amplitude and duration of the dendritic spike, including the degree of Na$^+$-channel inactivation and the strength of dendritic K$^+$ currents, similarly affected bursting and ADPs. Thus, dendritic Ca^{2+} channels could both increase (directly through their depolarizing current) and decrease (indirectly by activating Ca^{2+}-dependent K$^+$ channels) these phenomena. However, the effects of electrical structure on firing pattern and voltage trajectory were not strictly dependent on Ca^{2+}, as similar results could be obtained with a channel set lacking I_{Ca} and I_{KCa}, in

which interaction between I_{Na} and I_{Km} gave rise to bursts (not shown).

To relate the reconstructed multicompartmental models back to the reduced model we examined their electrotonic structure in more detail (Fig. 4). The neurons examined varied widely in both their dendritic membrane area and the degree of electrical attenuation between soma and dendrites. This can be seen in histograms of the steady-state electrical impedances between soma and dendritric compartments (see Fig. 4 legend). This metric is analogous to the parameter κ of the two-compartment model. Fast non-adapting spiking occurred for neurons with the smallest dendritic area and transfer impedances; adapting spike trains accompanied moderate dentritic area and transfer impedance; and bursting was associated with the largest dendritic area and transfer impedances. These findings are consistent with comparisons of electrical structure of 'thick' (bursting) and 'slender' (non-bursting) layer 5 cells[23] and with similarities in the developmental time course of electrical structure and electro-physiological properties of neocortical neurons[24].

Our results demonstrate that the electrotonic structure of a neuron shapes the dynamic interactions between non-uniformly distributed ion channels, and may thereby control the pattern of repetitive firing and the interspike membrane-potential trajectory. Heterogeneity of dendritic structure can thereby explain several aspects of the heterogeneous firing properties of neocortical neurons parsimoniously in terms of their anatomical variety.
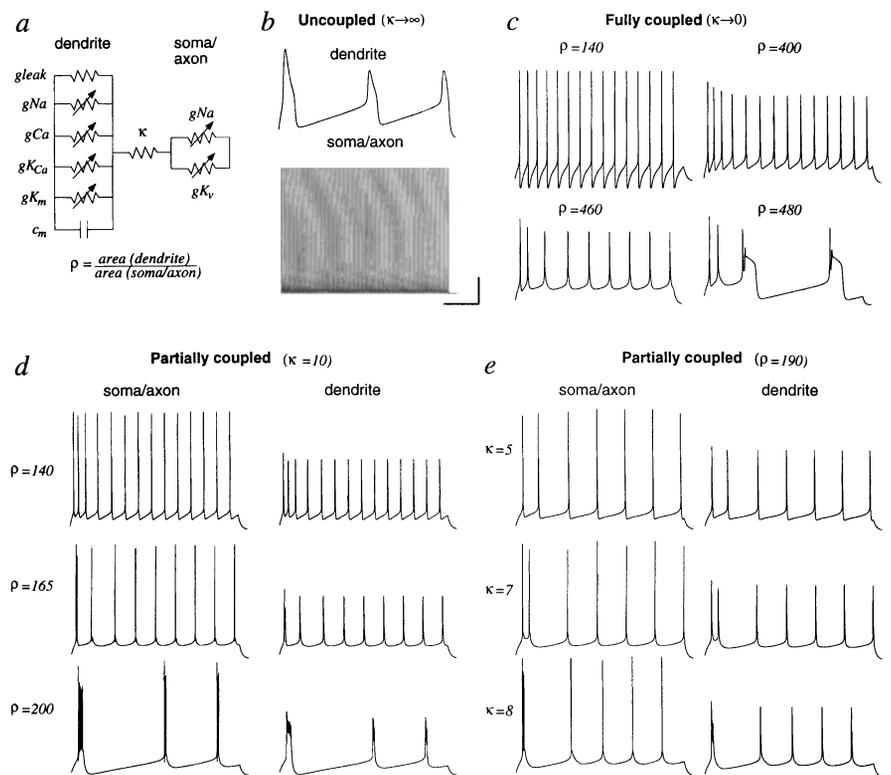
FIG. 1 Distinct firing patterns in model neurons with identical channel distributions but different dendritic morphology. Digital reconstructions of dendritic arborizations of neurons from rat somatosensory cortex (a) and cat visual cortex (b–d). a, Layer 3 aspiny stellate. b, Layer 4 spiny stellate. c, Layer 3 pyramid. d, Layer 5 pyramid. Somatic current injection (50, 70, 100, 200 pA for a–d, respectively) evoked characteristic firing patterns. a shows only the branch lengths and connectivity whereas b–d show a two-dimensional projection of the three-dimensional reconstruction. Scale bars: 250 μm (anatomy), 100 ms, 25 mV.

METHODS. Standard compartmental modelling techniques[26] were used to simulate spatially extended neurons with passive electrical structure, four voltage-dependent currents: fast Na$^+$, I_{Na} (refs 8,27); fast K$^+$, I_{Kv} (refs 8, 27); slow non-inactivating K$^+$, I_{Km} (ref. 28); and high-voltage activated Ca^{2+}, I_{Ca} (ref. 29) and one Ca^{2+}-dependent current, I_{KCa} (ref. 30). All dendritic branches were divided into cylindrical compartments with a maximum length of 50 μm. The dendritic membrane area of spiny neurons was increased to account for spines (adding 0.83 μm^2 per linear μm of dendrite). An axon, which was not present in the reconstructed anatomy, was attached to the soma of each cell[8]. The axon consisted of a conical hillock (10 μm long), tapering to one-quarter width to a cylindrical initial-segment region (15 μm) followed by 5 myelinated internodes (100 μm) separated by nodal segments. We took into account an observed correlation between soma diameter and initial segment diameter[30], by scaling the initial segment diameter as a function of the soma area. All currents were calculated using conventional Hodgkin–Huxley-style kinetics with an integration time step of 250 μs. Current (I) from each channel type was given by $I = \bar{g}a^x b(v - E)$, where $\bar{g}$ is the local conductance density, a is an activation variable with x order kinetics, b is an optional inactivation variable, v is the local membrane potential, and E is the reversal potential for the ionic species ($E_{leak} = -70$ mV, $E_K = -90$ mV, $E_{Na} = 50$ mV, $E_{Ca} = 140$ mV). Internal calcium concentration was computed using entry via I_{Ca} and removal by a first order pump: $d[Ca^{2+}]_i/dt = (-1 \times 10^5 \times I_{Ca}/2F) - ([Ca^{2+}]_i - [Ca^{2+}]_\infty)/\tau_R$, where $[Ca^{2+}]_\infty = 0.1$ μM, and $\tau_R = 200$ ms. Channel activation and inactivation variables were expressed in terms of a steady state value, $a_\infty(v)$, and a time constant $\tau_a(v)$ which were calculated from a first-order reaction scheme with forward rate α and backward rate β, giving $a_\infty(v) = \alpha/(\alpha(v) + \beta(v))$, $\tau_a = 1/(\alpha + \beta)$. The specific rate functions for each current were I_{Na} activation ($x = 3$): $\alpha = 0.182(v + 25)/(1 - e^{-(v+25)/9})$, $\beta = -0.124(V + 25)/(1 - E^{(V+25)/9})$; I_{Na} inactivation: $\alpha = 0.024(v + 40)/(1 - e^{-(v+40)/5})$, $\beta = -0.0091(v + 65)/(1e^{(v+65)/5})$, $b_\infty = 1/(1 + e^{(v+55)/6.2})$; I_{Ca} inactivation ($x = 2$): $\alpha = 0.055(v + 27)/(1 - e^{-(27+v)/3.8})$, $\beta = 0.94e^{-(v+75)/17}$; I_{Ca} inactivation: $\alpha = 4.57 \times 10^{-4} e^{-(v+13)/50}$, $\beta = 0.0065/(1 + e^{-(v+15)/28})$; I_{Kv} activation ($x = 1$): $\alpha = 0.02(v - 25)/(1 - e^{-(v-25)/9})$, $\beta = -0.002(v - 25)/(1 - e^{(v-25)/9})$; I_{Km} activation ($x = 1$): $\alpha = 1 \times 10^{-4}(v + 30)/(1 - e^{-(v+30)/9})$, $\beta = -1.10^{-4}(v + 30)/(1 - e^{(v+30)/9})$; I_{KCa} activation ($x = 1$): $\alpha([Ca^{2+}]_i) = 0.01 \times [Ca^{2+}]_i$, $\beta = 0.02$. Specific membrane capacitance (C_m) was


a

b

c

d
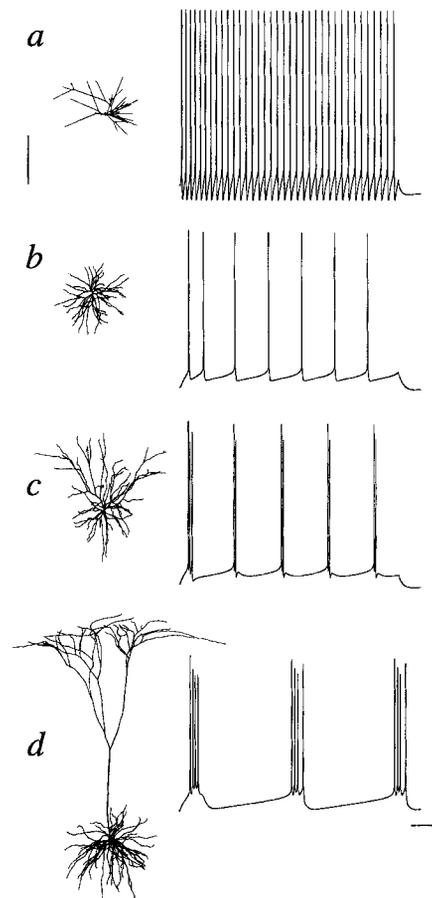
0.75 μF cm^{-2} (except myelinated axon segments, where $C_m = 0.02$ μF cm^{-2}). Specific membrane resistance (R_m) was 30 kΩ-cm^2 (except axon node segments, where $R_m = 50 \Omega - $cm^2). Specific axial resistance was 150 Ω-cm. Conductance densities (in pS μm^{-2}) were as follows. Dendrites: $\bar{g}_{Na} = 20$, $\bar{g}_{Ca} = 0.3$, $\bar{g}_{KCa} - = 3$, and $\bar{g}_{Kv} = 0.1$. Soma: as dendrites and in addition $\bar{g}_{Kv} = 200$. Axon hillock and initial segment: $\bar{g}_{Kv} = 2000$, $\bar{g}_{Na} = 30,000$. Nodes of Ranvier: $\bar{g}_{Na} = 30,000$. The rates and conductance densities were developed at 23 °C and were therefore increased from the values given to 37 °C using a Q_{10} of 2.3.

FIG. 2 Effects of electrical structure on firing pattern in a reduced model. *a*, A two-compartment model incorporating the same channels modelled in Fig. 1. The two compartments correspond to the dendritic tree ('dendrite') and the soma and axon initial segment ('axon–soma'). The parameter κ specifies the electrical resistance (coupling) between the two compartments. The parameter ρ specifies the ratio of dendritic to axo–somatic area and thereby sets the strength of dendritic currents relative to axo–somatic currents. The channels and membrane properties of each compartment are depicted. *b*, Uncoupled dendritic (top) and axo-somatic (bottom) compartments ($\kappa \rightarrow \infty$) are each capable of discharging repetitively when current is injected (top, 400 pA; bottom, 10 pA). Note that the firing frequency of the axo-somatic compartment, which is driven by the fast I_{Na} and I_{Kv} is much higher than for the dendritic compartment, which is driven by I_{Ca}, I_{KCa} and I_{Km}. *c*, When fully coupled ($\kappa \rightarrow 0$), eliminating electrotonic effects, the amount of spike-frequency adaptation varies with the size of the dendritic compartment, but the model does not display bursting or spike ADPs. *d*, *e*, Partial coupling produces voltage gradients between axo-somatic (left) and dendritic (right) compartments and supports bursting and ADPs. When partially coupled, changes in either dendritic area ρ (*d*) or changes in coupling κ (*e*) alter firing pattern to injected current (100 pA, injected in axo–somatic compartment). Scale bar (30 mV, 200 ms) applies to all panels.

METHODS. Compartmental simulations were carried out with channels described in Fig. 1. The dendritic compartment properties were: $C_m = 0.75\,\mu F\,cm^{-2}$, $R_m = 30\,k\Omega - cm^2$, and active conductances (in pS μm^{-2}) $\bar{g}_{Na} = 15$, $\bar{g}_{Ca} = 0.3$, $\bar{g}_{KCa} = 3$, and $\bar{g}_{Km} = 0.1$. The axo–somatic compart-

ment contained just $\bar{g}_{Kv} = 1500$, $\bar{g}_{Na} = 30{,}000$. The compartments were connected with axial resistance given by the parameter κ, which generally ranged from 1 to 10 MΩ. The area of the axo–somatic compartment was $100\,\mu m^2$ and the area of the dendritic compartment was specified as a multiple (ρ) of the axo–somatic area, generally 100 to 500. Presence of a leak conductance and capacitance in the axo–somatic compartment did not affect the results and were therefore omitted for simplicity.
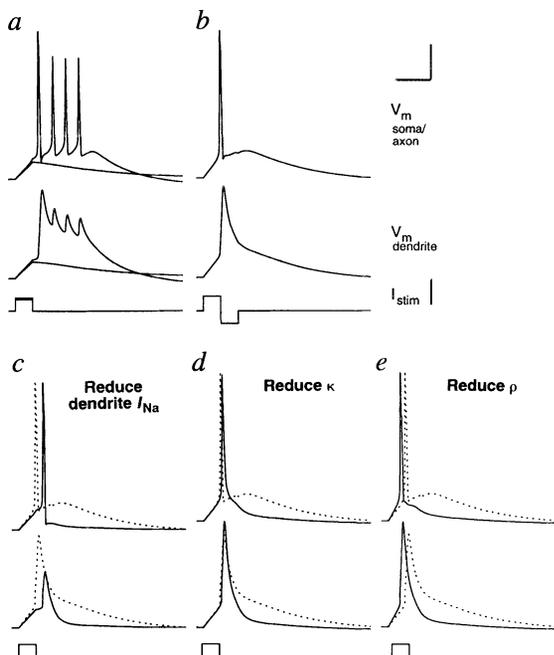
FIG. 3 Electrical basis for spike after-depolarization and bursting in the reduced model. *a*, All-or-none bursting in a partially coupled two-compartment model ($\rho = 200$, $\kappa = 10$) was triggered by a short current pulse. Just subthreshold and superthreshold responses are shown. *b*, The burst could be suppressed after the first spike when followed by a short hyperpolarizing pulse. This revealed an underlying depolarizing envelope driven by a prolonged dendritic spike. *c*, Reducing the dendritic Na$^+$ conductance by 70% reduced the width and amplitude of the dendritic spike and suppressed burst generation and the depolarizing potential following the spike. Reducing the electrical coupling κ (*d*, 50% reduction) or the ratio of dendritic to axo-somatic area ρ (*e*, 30% reduction) also substantially reduced the sustained depolarization. In each panel, voltage of the axon–soma (top) and the dendrite (centre) and the stimulus (bottom) are shown. In panels c–e, the control condition *b* is shown in dotted lines for comparison. Scale bars (20 ms, 30 mV, 1 nA) apply to all panels.
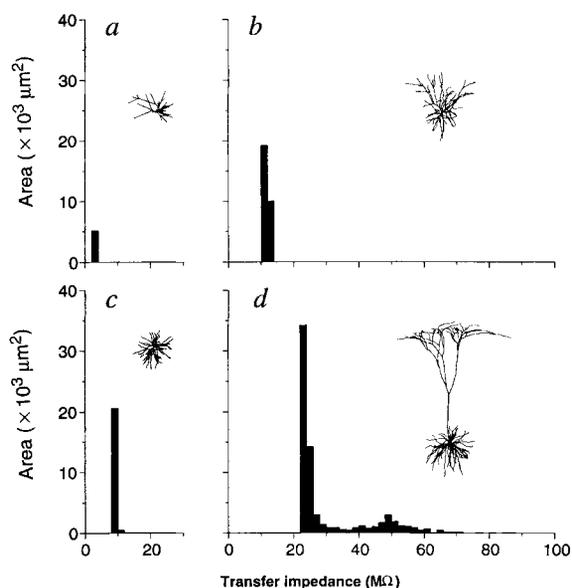
FIG. 4 Electrical geometry of cortical cells. Histograms show the distribution of electrical attenuation between the soma and dendritic segments for the four neurons depicted in Fig. 1. The steady-state transfer impedance (Z) from the soma to each simulated dendritic compartment was calculated by injecting a small current step (I) in the soma and measuring the resulting (passive) steady-state voltage change (V) in the dendritic compartment ($Z = V/I$). The histogram bin corresponding to this impedance level was then incremented by an amount equal to the membrane area of that compartment. The total area of the histogram therefore reflects the total dendritic area and the shape of the histogram reflects the relative electrical distance of the dendritic membrane from the soma. These can be compared to the parameters ρ and κ in the reduced model, respectively.

Direct experimental tests of this model could be made by partial dendritic ablation or manipulations to alter cytoplasmic resistivity.

As there is a wide anatomical variety of neocortical dendrites[1], our findings support the idea of a continuous spectrum of neo-cortical firing patterns[2,3] rather than discrete categories. Differences in spike shape[2,24] passive response properties[24], and some aspects of the time course of adaptation[25] observed *in vitro* were not readily reproduced in the present model. These limitations indicate that differences in channel types or intracellular Ca^{2+} dynamics may also be important. Thus, although the present study does not exclude contributions of differential channel expression or other physiological differences, it supports the hypothesis that neocortical neurons that share similar channel distributions may derive functional differentiation from their dendritic morphology. Similar principles may also apply to other mophologically heterogeneous neuronal populations. □

1. Peters, A. & Jones, E. G. Cerebral Cortex Vol 1: Cellular Components of the Cerebral Cortex (Plenum, New York, 1984).
2. McCormick, D. A., Connors, B. W., Lighthall, J. W. & Prince, D. A. J. Neurophysiol. **54**, 782–806 (1985).
3. Connors, B. W. & Gutnick, M. J. Trends Neurosci. **13**, 99–104 (1990).
4. Chagnac-Amitai, Y., Luhmann, H. J. & Prince, D. A. J. comp. Neurol. **296**, 598–613 (1990).
5. Mason, A. & Larkman, A. U. J. Neurosci. **10**, 1415–1428 (1990).
6. Franceschetti, S., Guatteo, E., Panzica, F., Sancini, G. E. W. & Avanzini, G. Brain Res. **696**, 127–139 (1995).
7. Yang, C. R., Seamans, J. K. & Gorelova, N. J. Neurosci. **16**, 1904–1921 (1996).
8. Mainen, Z. F., Joerges, J., Huguenard, J. R. & Sejnowski, T. J. Neuron **15**, 1427–1439 (1995).
9. Yuste, R. & Tank, D. W. Neuron **16**, 701–716 (1996).
10. Rapp, M., Yarom, Y. & Segev, I. Proc. natn. Acad. Sci. U.S.A. (in the press).
11. Stuart, G. J. & Sakmann, B. Nature **367**, 69–72 (1994).
12. Wollner, D. A. & Catterall, W. A. Proc. natn. Acad. Sci. U.S.A. **83**, 8424–8428 (1986).
13. Angelides, K. J., Elmer, L. W., Loftus, D. & Elson, E. J. Cell Biol. **106**, 1911–1924 (1988).
14. Schwindt, P. C. et al. J. Neurophysiol. **59**, 424–449 (1988).
15. Storm, J. F. Prog. Brain Res. **83**, 161–187 (1990).
16. Kim, H. G. & Connors, B. W. J. Neurosci. **13**, 5301–5311 (1993).
17. Yuste, R., Gutnick, M. J., Saar, D., Delaney, R. D. & Tank, D. W. Neuron **13**, 23–43 (1994).
18. Pinsky, P. F. & Rinzel, J. J. comput. Neurosci. **1**, 39–60 (1994).
19. Turner, R. W., Maler, L., Deerinck, T., Levinson, S. R. & Ellisman, M. H. J. Neurosci. **14**, 6453–6471 (1994).
20. Azouz, R., Jensen, M. S. & Yaari, Y. J. Physiol. **492**, 211–223 (1996).
21. Granit, R., Kernell, D. & Smith, R. S. J. Physiol. **168**, 100–115 (1963).
22. Kandel, E. R. & Spencer, W. A. J. Neurophysiol. **24**, 243–259 (1961).
23. Larkman, A. U., Major, G., Stratford, K. J. & Jack, J. J. B. J. comp. Neurol. **323**, 137–152 (1992).
24. Kasper, E. M., Larkman, A. U., Lubke, J. & Blakemore, C. J. comp. Neurol. **339**, 475–494 (1994).
25. Agmon, A. & Connors, B. W. J. Neurosci. **12**, 319–329 (1993).
26. Hines, M. In Neural Systems: Analysis and Modeling (ed. Eeckman, F. H.) 127–136 (Kluwer, Boston, MA, 1993).
27. Hamill, O. P., Huguenard, J. R. & Prince, D. A. Cerebral Cortex **1**, 48–61 (1991).
28. Gutfreund, Y., Yarom, Y. & Segev, I. J. Physiol. **483**, 621–640 (1995).
29. Reuveni, I., Friedman, A., Amitai, Y. & Gutnick, M. J. J. Neurosci. **13**, 4609–4621 (1993).
30. Sloper, J. J. & Powell, T. P. S. Phil. Trans. R. Soc. Lond. **B285**, 173–197 (1978).

Critical role for β7 integrins in formation of the gut-associated lymphoid tissue

Norbert Wagner*, Jürgen Löhler†, Eric J. Kunkel‡, Klaus Ley‡, Euphemia Leung§, Geoff Krissansen§, Klaus Rajewsky* & Werner Müller*

* Institute for Genetics, University of Cologne, 50937 Cologne, Germany
† Heinrich-Pette-Institute for Experimental Virology and Immunology, University of Hamburg, 20251 Hamburg, Germany
‡ Department of Biomedical Engineering, University of Virginia, Charlottesville, Virginia 22908, USA
§ Department of Molecular Medicine, University of Auckland, Auckland, New Zealand

IMMUNE defence against pathogens entering the gut is accomplished by lymphocytes in the gut-associated lymphoid tissue (GALT), a major compartment of the immune system[1]. The GALT, comprising Peyer's patches, lamina propria lymphocytes and intra-epithelial lymphocytes of the intestine, is populated by lymphocytes that migrate there from the vasculature[2,3]. Here we report that, in mice deficient for the β7 integrin subfamily of adhesion molecules, the formation of the GALT is severely impaired. This is probably due to a failure of β7$^{-/-}$ lymphocytes to arrest and adhere to the vasculature at the site of transmigration into the GALT.

Lymphocytes move through the GALT by means of differential expression and activation of adhesion molecules[4]. Emigration of lymphocytes from the vasculature into tissues requires them to roll along the endothelial cells, arrest and adhere firmly to endothelial cells, and migrate across the endothelium[5,6].

The β7 integrin subfamily of adhesion molecules is expressed on a subset of lymphocytes, and consists of two members, α4β7 and αEβ7 (refs 7–10): α4β7 mediates the adherence of lymphocytes to high endothelial venules (HEVs) of Peyer's patches[11] and has been implicated in lymphocyte rolling[12], and αEβ7 mediates the adherence of intra-epithelial lymphocytes of the intestine (IELs) to the intestinal epithelium[13]. In chronic inflammatory bowel disease, either α4β7 or α4β1, or both, mediates the migration of lymphocytes into inflammatory lesions[14]. To analyse the contribution of the β7 integrins to the formation of the GALT, and to determine how β7 integrins participate in the compartmentalization of the immune system, we generated β7-deficient mice.